Volume 16, Issue 2, 162502 (1-10)

International Journal of Industrial Chemistry (IJIC)

https://doi.org/10.57647/j.ijic.2025.1602.09

Synthesis and Characterization of Copper Ferrite and Manganese Ferrite Nanoparticles and their Toxicity on Breast Cancer Cells

Mehdi Abdollahzadeh Parsa[1], Fereshteh Rahmati[1*], Fatemeh Molaabasi[2], Saman Hosseinkhani[3]

[1]Department of Biochemistry, NT.C., Islamic Azad University, Tehran, Iran
[2]Medical Nanotechnology Group, Department of Interdisciplinary Technologies, Breast Cancer Research Center, Motamed Cancer Institute, ACECR, Tehran 1517964311, Iran
[3]Department of Biochemistry, Faculty of Biological Sciences, Tarbiat Modares University, Tehran, Iran

[*]**Corresponding author:** fereshtehrahmati12345@iau.ac.ir

Research Article
Received:
21 August 2025
Revised:
25 September 2025
Accepted:
13 October 2025
Published in Issue:
30 June 2025

Abstract:

Ferrite nanoparticles (NPs) have emerged as promising candidates for cancer treatment due to their unique magnetic properties and biocompatibility, which facilitate targeted drug delivery. This study focuses on the synthesis of copper ferrite ($CuFe_2O_4$) and manganese ferrite ($MnFe_2O_4$) nanoparticles using a hydrothermal method, and assesses their cytotoxic effects on human breast cancer (MCF-7) cells. Characterization techniques, including X-ray diffraction (XRD), scanning electron microscopy (SEM), energy-dispersive X-ray spectroscopy (EDX), Fourier transform infrared (FTIR) spectroscopy, ultraviolet–visible (UV–Vis) spectroscopy, and vibrating sample magnetometry (VSM), confirmed the successful formation of pure spinel structures. XRD patterns aligned with standard references, while SEM images indicated nearly spherical shapes, with average diameters of 145 nm for $CuFe_2O_4$ and 170 nm for $MnFe_2O_4$. EDX analysis validated elemental composition, and FTIR spectra showed characteristic metal–oxygen vibrations. UV–Vis spectra exhibited specific peaks for both ferrites, highlighting charge-transfer transitions. Magnetic analysis revealed ferromagnetism, with $MnFe_2O_4$ exhibiting a higher saturation magnetization. In vitro assays showed that $CuFe_2O_4$ significantly reduced the viability of MCF-7 cells in a dose-dependent manner, suggesting its potential as a biocompatible candidate for targeted breast cancer therapy. Additional research is needed to discover mechanisms of action and in vivo efficacy.

Keywords: Copper ferrite, Manganese ferrite, Nanoparticles, Breast cancer, Cytotoxicity, Magnetic properties

---

Cite this article: Abdollahzadeh Parsa, M., Rahmati, F., Molaabasi, F., & Hosseinkhani, S. (2025). Synthesis and characterization of copper ferrite and manganese ferrite nanoparticles and their toxicity on breast cancer cells, *International Journal of Industrial Chemistry*, 16(2). 1-10 https://doi.org/10.57647/j.ijic.2025.1602.09

1. Introduction

Nanotechnology has become one of the most dynamic research areas in modern science, exerting a profound influence on human life. The field of cancer therapeutics has seen extensive research into various nanomaterials and nanocarriers, including synthetic polymers, lipid-based systems, protein carriers, organic and inorganic compounds, glycans, and metallic nanoparticles. Nanocarriers offer several essential advantages for drug delivery, including enhanced absorption, improved bioavailability, protection from metabolic degradation, increased solubility, better tissue distribution, and targeted delivery through both active and passive mechanisms [1-4]. Nanomedicines can also help overcome drug resistance by extending circulation time and enhancing cellular uptake [5]. However, challenges remain, including manufacturing inconsistencies, metabolic limitations, potential dose dumping, and limited drug-loading capacity. Among NPs, magnetic NPs are particularly valuable due to their small size, stability, ease of functionalization, and unique optical properties. These magnetic NPs are used in drug delivery, magnetic resonance imaging (MRI), radiation therapy, diagnostics, tumor imaging, and early cancer detection [6, 7]. Their ability to alter pharmacokinetic and pharmacodynamic properties, improve drug solubility, enhance stability, and enable targeted delivery while reducing side effects makes them especially useful for cancer treatment [8, 9].

In recent years, ferrite nanoparticles have emerged as promising candidates for biomedical applications due to their distinctive magnetic properties, catalytic activity, and biocompatibility. Ferrites, a class of magnetic oxides, typically exist as powders or ceramics with ferromagnetic characteristics [10, 11]. Mainly composed of iron oxides, these materials may have ferric and ferrous ions partially substituted with other transition metals [12]. Key iron oxides include magnetite (Fe_3O_4) and maghemite (γ-Fe_2O_3), with magnetite exhibiting an inverse spinel ferrite structure. The general formula for spinel ferrites is MFe_2O_4, where M represents a metal cation [8].

Notably, $CuFe_2O_4$ and $MnFe_2O_4$ NPs have demonstrated exceptional potential in cancer therapy due to their tunable magnetic properties, chemical stability, and ability to induce oxidative stress in cancer cells [13-15]. Breast cancer is one of the most common and deadly cancers worldwide, and conventional treatments such as chemotherapy or radiotherapy often have severe side effects and drug resistance. Magnetic NPs offer a compelling alternative therapeutic and diagnostic approach by enabling targeted drug delivery, hyperthermia therapy, photothermal therapy, and the induction of reactive oxygen species (ROS)-mediated apoptosis [16, 17]. For example, Manivasagan et.al investigated the photothermal therapeutic potential of calcium-doped magnesium ferrite nanoparticles (Ca^{2+}-$MgFe_2O_4$ NPs) on the human breast adenocarcinoma (MDA-MB-231) cell line. The synthesized NPs exhibited a uniform spherical morphology, with a mean diameter of 14.24 nm, and demonstrated a photothermal conversion efficiency of 30.12%. In in vitro assays, no significant cytotoxicity was observed in MDA-MB-231 cells without laser irradiation. Interestingly, Ca2+-MgFe2O4 NPs exhibited greater cytotoxicity toward laser-irradiated MDA-MB-231 cells, resulting in increased cell death [18].

Beyond their unique optical and magnetic properties, ferrite NPs have gained attention due to their capacity for chemical modification through adjustments in their initial composition or cation substitution [19]. The biocompatibility of ferrite NPs was also confirmed by Kuckelhouse et al., who examined cobalt-ferrite-based magnetic fluid and magnetoliposomes [20]. Baldi et al. reported hyperthermic applications of cobalt ferrite NPs [21], while Lin et al. investigated the effect of $Mn_{0.5}Zn_{0.5}Fe_2O_4$ NPs on hepatocellular carcinoma (HCC) cells [22]. In another study, the cytotoxicity of nickel–zinc (NiZn) ferrite NPs was evaluated against three cancer cell lines: human colon cancer (HT29), human breast cancer (MCF7), and human liver cancer (HepG2) cells. The 3 (4,5-dimethylthiazol-2-yl) 2,5-diphenyltetrazolium bromide (MTT) assay—a colorimetric method for assessing cell viability based on mitochondrial metabolic activity—indicated dose-dependent growth inhibition at concentrations ranging from 15.6 to 1000 µg/mL for 72 h. Apoptotic effects were further evidenced by increased activation of caspases 3/9 (CASP3/9) and DNA fragmentation, confirming the significant cytotoxic potential of NiZn ferrite NPs, particularly against HepG2 cells [23]. Moreover, nickel (Ni) ferrite NPs induced dose-dependent cytotoxicity in both HepG2 and MCF-7 cells by generating ROS, depleting glutathione (GSH), and causing lipid peroxidation along with mitochondrial membrane disruption. At the molecular level, Ni ferrite NPs downregulate the expression of anti-apoptotic gene BCL2 (B cell lymphoma 2). Conversely, they upregulate the pro-apoptotic genes, including p53, Bax (BCL2-associated X), and CASP3/9. Comparative analysis revealed that MCF-7 cells were more sensitive to Ni ferrite NPs than HepG2 cells [24]. Zinc nanoparticles (Zn NPs) were also evaluated for cytotoxicity against human lung epithelial cancer (A549), human skin epithelial cancer (A431), and HepG2 cells. These NPs, with a mean size of 44 nm, induced cytotoxic effects in a concentration-dependent manner (10–40 µg/mL), accompanied by increased ROS levels, reduced GSH, collapse of mitochondrial membrane potential (MMP), upregulation of p53, Bax, and CASP3/9, and downregulation of BCL-2 [25].

In this study, $CuFe_2O_4$ and $MnFe_2O_4$ nanoparticles (NPs) were synthesized using a hydrothermal method, followed by comprehensive characterization of their structural, morphological, and magnetic properties. Their cytotoxic effects on MCF-7 cells were subsequently evaluated, revealing a significant difference in anticancer activity between the two types of ferrite.

2. Materials and Methods

2.1. Materials

Copper (II) chloride dihydrate ($CuCl_2·2H_2O$), manganese (II) chloride dihydrate ($MnCl_2·2H_2O$), ferric chloride hexahydrate ($FeCl_3·6H_2O$), trisodium citrate dihydrate ($Na_3Cit·2H_2O$), sodium acetate (NaAc), ethanol (C_2H_6O, 99%), dimethyl sulfoxide (DMSO) and ethylene glycol (EG) were obtained from Merck (Darmstadt, Germany). All chemicals were of analytical grade and used without further purification. Materials for cell culture, including Dulbecco's Modified Eagle Medium (DMEM), phosphate-buffered saline (PBS) tablets, trypsin, penicillin–streptomycin (Pen-Strep) antibiotic, and fetal bovine serum (FBS), were purchased from Sigma-Aldrich (St. Louis, MO, USA) and Gibco (Grand Island, NY, USA).

2.2. Structural characterization and evaluation of NPs

The structural and physicochemical properties of ferrite NPs were analyzed using various characterization techniques. Optical properties were measured using a UV–Vis spectrophotometer (UV-1700, Shimadzu, Japan). Magnetic properties were assessed using a vibrating sample magnetometer (VSM; MDKB, Magnetic Daghigh Kavir Co., Iran) at room temperature. Functional groups and chemical bonds were identified via Fourier-transform infrared spectroscopy (FTIR; 8500S, Shimadzu, Japan). Surface morphology and particle size were examined using field-emission scanning electron microscopy (FE-SEM; Sigma 300, ZEISS, Germany). Crystal structure and phase purity were determined by X-ray diffraction (XRD) using a Philips PW 1730/10 diffractometer (Philips, Holland) equipped with Cu-Kα radiation.

2.3. Synthesis of ferrite NPs based on the hydrothermal method

First, for the synthesis of $CuFe_2O_4$, $FeCl_3·6H_2O$ (1.28 g), $NaAc·3H_2O$ (2.63 g), $NaCit·2H_2O$ (0.01 g), and copper chloride precursor ($CuCl_2·2H_2O$ (0.41 g) were mixed in 32 mL of ethylene glycol (pH = 7.4). This protocol was also carried out for the synthesis of $MnFe_2O_4$ with 0.384 g of $MnCl_2·2H_2O$. Next, the mixtures were stirred for 2 h at room temperature. During the hydrothermal reaction, the solutions were placed in an autoclave cylinder and heated to 200°C for 12 h. Purification of the NPs was done by washing three times with distilled water, followed by three washes with 99% ethanol. Finally, the NPs were dried at 40°C for 3 h and stored in a sealed glass container.

2.4. Culturing MCF7 cells and evaluation of NPs cytotoxicity on MCF7 cells

The MCF-7 cells (purchased from the Motamed Cancer Institute, Tehran, Iran) were grown in DMEM medium containing 10% FBS and 1% Pen-Strep antibiotic. The cells were placed in a humidified incubator at 37°C with 5% CO_2. To assess cytotoxicity, MCF-7 cells were seeded in 96-well plates at a density of 10^4 cells per well and allowed to adhere for 24 h. The cells were then exposed to varying concentrations of nanoparticles (0.01, 0.02, 0.04, 0.08, 0.1, and 0.2 mg/mL) for an additional 24 h. Before incubation, the NP suspensions were sonicated to ensure proper dispersion. After the treatment, an MTT solution (0.5 mg/mL) was added, and the samples were incubated for an additional 3 h. Subsequently, the formazan crystals were dissolved in DMSO, and their absorbance at 570 nm was measured.

2.5 Statistical analysis

Statistical analysis and data visualization were conducted using GraphPad Prism version 8.2.1 (GraphPad Software, Inc., San Diego, CA, USA). The results are expressed as mean ± standard deviation (SD). A one-way ANOVA was utilized to compare the groups, followed by a Newman–Keuls multiple comparison post-hoc test. A significance level of $p \leq 0.05$ was established.

3. Results and discussion

3.1. SEM and EDX analysis of $CuFe_2O_4$ and $MnFe_2O_4$ NPs

SEM images revealed that the NPs exhibit spherical morphology, with an average particle diameter of approximately 145 nm for $CuFe_2O_4$ (Fig. 1a) and 170 nm for $MnFe_2O_4$ (Fig. 1b). EDX analysis confirmed the presence of O, Fe, and Cu in $CuFe_2O_4$ NPs with weight percentages of 57.76%, 29.15%, and 13.09%, respectively (Fig. 1a), and O, Fe, and Mn in $MnFe_2O_4$ NPs with weight percentages of 57.91%, 29.11%, and 12.98%, respectively (Fig. 1b).

According to previous reports, ferrite NPs smaller than 200 nm do not interfere with their biomedical applications. For instance, Vurro et al. synthesized citrate- and glucose-coated ferrite NPs with hydrodynamic sizes ranging from ~100–300 nm, which were employed as MRI and magnetic particle imaging (MPI) contrast agents, as well as antitumor agents in magnetic fluid hyperthermia (MFH) targeting MDA-MB-231 cells [26]. Similarly, Al Gburi et al. developed $Cu_{0.5}Zn_{0.5}Fe_2O_4$ NPs with a microstructural size distribution of 20–200 nm and proposed them as potential hyperthermia agents in cancer treatment [14].

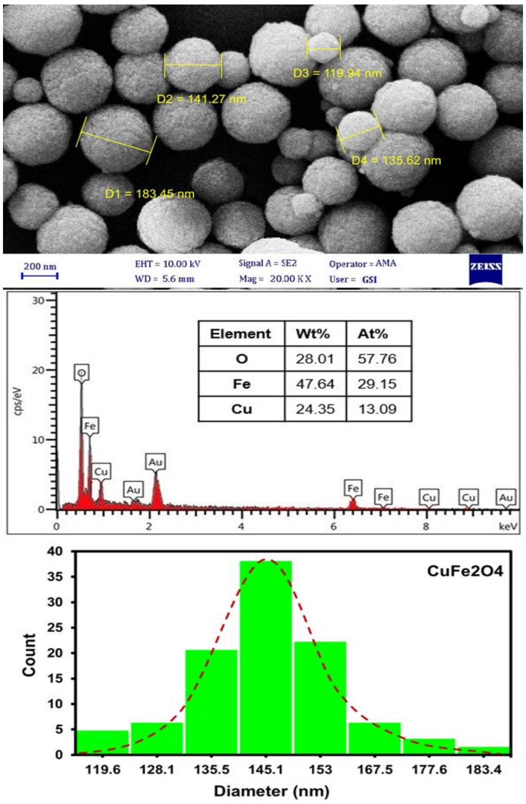

Element	Wt%	At%
O	28.01	57.76
Fe	47.64	29.15
Cu	24.35	13.09

Figure 1a. SEM, EDX, and size distribution analysis of $CuFe_2O_4$ NPs. The results were recorded at an accelerating voltage of 10 kV and a working distance of 5.6 mm, with a magnification of 20,000×. The scale bar corresponds to 200 nm

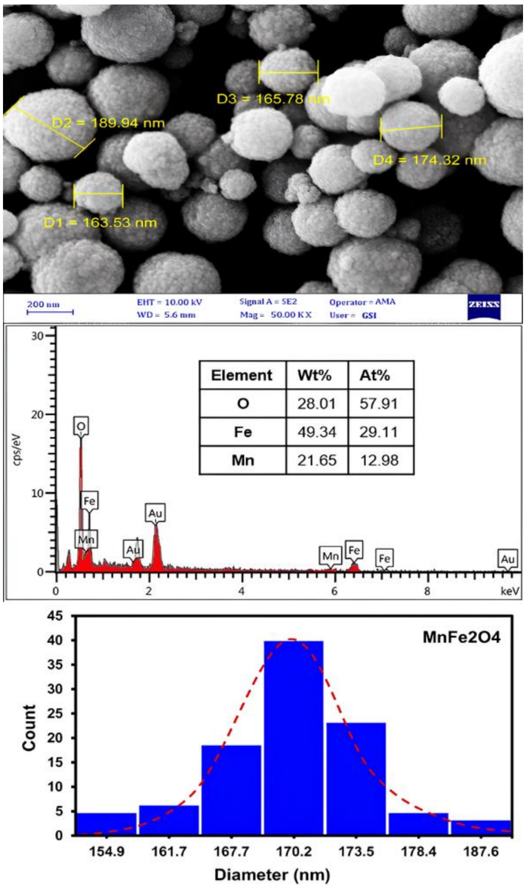

Element	Wt%	At%
O	28.01	57.91
Fe	49.34	29.11
Mn	21.65	12.98

Figure 1b. SEM, EDX, and size distribution analysis of $MnFe_2O_4$ NPs. The results were recorded at an accelerating voltage of 10 kV and a working distance of 5.6 mm, with a magnification of 50,000×. The scale bar corresponds to 200 nm

3.2. UV-Visible analysis of $CuFe_2O_4$ and $MnFe_2O_4$ NPs

The optical absorption spectra of NPs were recorded in the range of 200–900 nm (Fig. 2). For $CuFe_2O_4$, a distinct absorption peak appeared at 285 nm, corresponding to charge-transfer transitions between oxygen ions (O^{2-}) and metal ions (Cu^{2+} or Fe^{3+}), indicating strong electronic interactions within the spinel structure. A relatively weaker absorption band was observed at 711 nm, attributed to the d-d transitions of Cu^{2+} and Fe^{3+} ions. Although typically less intense and broader than charge-transfer bands, d–d transitions contribute significantly to the optical and magnetic properties of ferrite NPs. The presence of both absorption features confirms the successful synthesis and characteristic spinel structure of $CuFe_2O_4$ NPs. For $MnFe_2O_4$, a distinct absorption peak was observed at 297 nm, also corresponding to charge-transfer transitions between oxygen ions (O^{2-}) and metal ions (Mn^{2+} or Fe^{3+}) within the spinel structure. This peak reflects strong electronic interactions between oxygen and metal atoms. A weaker absorption band at 701 nm was attributed to the d-d transitions of Mn^{2+} and Fe^{3+} ions. Although typically less intense and broader than charge-transfer bands, these d–d transitions significantly contribute to the magnetic and optical properties of ferrite NPs. The presence of both absorption features at 297 and 701 nm confirms the successful synthesis and characteristic spinel structure of $MnFe_2O_4$ Nps (Fig. 2).

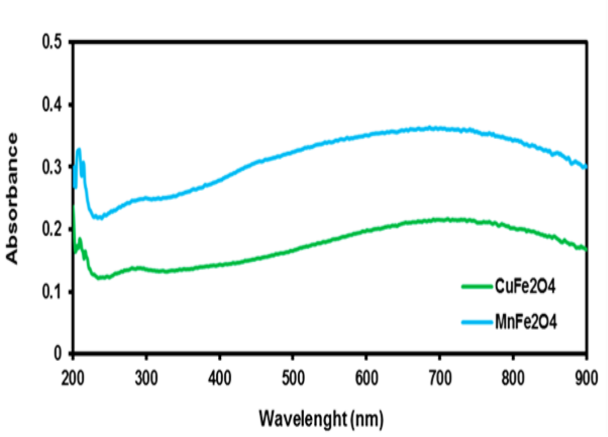

Figure 2. UV-vis analysis of $CuFe_2O_4$ and $MnFe_2O_4$ nanoparticles

3.3. FTIR analysis of $CuFe_2O_4$ and $MnFe_2O_4$ NPs

The FTIR spectra of the NPs were recorded in the range of 370–4000 cm⁻¹ (Fig. 3), and the major absorption peaks are summarized in Table 1. Distinct peaks at 591 cm⁻¹ and 389 cm⁻¹ confirmed the formation of the $CuFe_2O_4$ spinel structure, while corresponding peaks at 589 cm⁻¹ and 406 cm⁻¹ indicated the formation of the $MnFe_2O_4$ spinel structure. In line with previous reports, both spectra exhibited a broad absorption band at 3412 cm⁻¹ and a distinct band at 1718 cm⁻¹, indicating the presence of surface O–H groups or adsorbed moisture [26]. Metal-oxygen (M–O) vibrations generally appear below 1000 cm⁻¹, with peaks under 700 cm⁻¹ being characteristic of the spinel structure. Notably, the absorption band near 539 cm⁻¹ corresponds to intrinsic vibrations of octahedrally coordinated metal ions, further confirming the successful formation of a spinel ferrite phase [27, 28].

Table 1. FTIR spectrum of $CuFe_2O_4$ and $MnFe_2O_4$ nanoparticles

Ferrites	Peak (cm⁻¹)	Vibration Mode	Assignment
$CuFe_2O_4$	3423.6	ν(O–H)	Stretching of hydroxyl groups (adsorbed moisture/surface –OH)
	2925.7	ν(C–H)	Stretching of C–H bonds (residual organics: surfactants/solvents)
	1644.4	δ(H–O–H)	Bending of adsorbed water molecules
	1415.5	δ(C–O), ν(C–O–H)	Bending of C–O groups or residual nitrates/carbonates
	1040	ν(C–O)	Stretching of C–O bonds (organic residues)
	591.3	ν(Fe–O)	Octahedral (B) site in $CuFe_2O_4$ spinel
	389.8	ν(Cu–O)	Tetrahedral (A) site in $CuFe_2O_4$ spinel
$MnFe_2O_4$	3426.7	ν(O–H)	Stretching of hydroxyl groups (adsorbed moisture/surface –OH)
	2928.7	ν(C–H)	Stretching of C–H bonds (residual organics)
	1639.8	δ(H–O–H)	Bending of adsorbed water molecules
	1413.9	δ(C–O), ν(C–O–H)	Bending of C–O groups or residual nitrates/carbonates
	1050.7	ν(C–O)	Stretching of C–O bonds (organic residues)
	589.8	ν(Fe–O)	Tetrahedral (A) site in $MnFe_2O_4$ spinel
	406.6	ν(Mn–O)	Octahedral (B) site in $MnFe_2O_4$ spinel

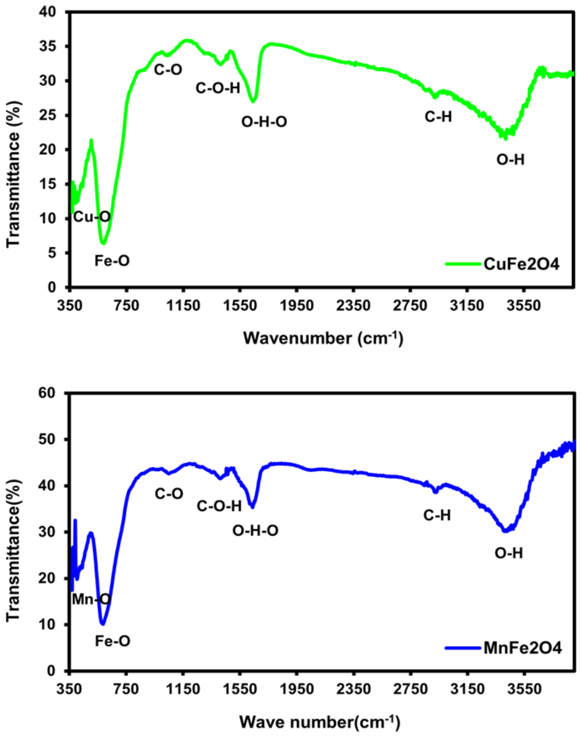

Figure 3. FTIR spectrum of $CuFe_2O_4$ and $MnFe_2O_4$ nanoparticles

3.4. XRD analysis of $CuFe_2O_4$ and $MnFe_2O_4$ NPs

The XRD pattern of $CuFe_2O_4$ NPs was recorded in the 2θ range of 10-80°. Distinct peaks matched the standard pattern of copper ferrite (JCPDS 34-0425), confirming the formation of a spinel structure. The primary diffraction peaks appeared at approximately 18.4°, 30.2°, 35.6°, 43.3°, 50.48°, 57.2°, 62.9°, and 74.4° corresponding to the (111), (220), (311), (400), (422), (511), (440), and (533) crystallographic planes, respectively. The peak at (111) indicates the primary crystalline order in low-angle planes, while the (220) peak provides information on atomic distances and crystalline ordering. The (311) reflection at (2θ ≈ 35.6°) is characteristic of the spinel structure and reflects high crystallinity. The (400) peak suggests an appropriate crystal symmetry, and the (422) reflection supports the well-ordered crystalline arrangement, with intensities influenced by nanoparticle size and crystal quality. The (440) peak is typical of $CuFe_2O_4$ spinel phase, indicating crystal orientation in higher-energy planes and supporting structural purity. Additionally, the (511) peak is a secondary plane where diffraction typically occurs with medium to low intensity, contributing to the completion and confirmation of the spinel structure. Peaks at (511) and (533) correspond to secondary and high-angle planes, respectively, both of which contribute to the confirmation of long-range crystalline order and the absence of impurities.

The XRD pattern of $MnFe_2O_4$ NPs also exhibited the distinct peaks matching the standard pattern of manganese ferrite (JCPDS 10-0319), consistent with a spinel structure. Prominent peaks appeared at approximately 18.3°, 30.2°, 35.5°, 43.2°, 53.5°, 57°, 62.6°, and 73.96° corresponding to the (111), (220), (311), (400), (422), (511), (440), and (533) crystal planes, respectively. The (111) reflection, though low in intensity, indicated the initial ionic arrangement within the lattice. The (220) peak, with medium intensity, reflects crystal growth along specific crystalline planes, supporting the cubic structure and confirming the regular arrangement of Mn^{2+} ions in the lattice. The (311) peak, the most prominent reflection in spinel ferrites, exhibited high intensity, signifying a dominant spinel phase and well-crystallized NPs. The (400) and (422) reflections confirm the structural symmetry and optimal ion distribution. The (440) peak supports the absence of secondary phases, while the (511) peak indicates uniform crystallites with no detectable impurities. The high-angle (533) peak confirms the presence of a long-range order in the crystal lattice. Notably, the most intense diffraction peak of $MnFe_2O_4$ was observed at $2\theta \approx 35.5°$ corresponding to the (311) reflection, confirming the dominance of the spinel phase and high-quality NP crystallization (Fig. 4).

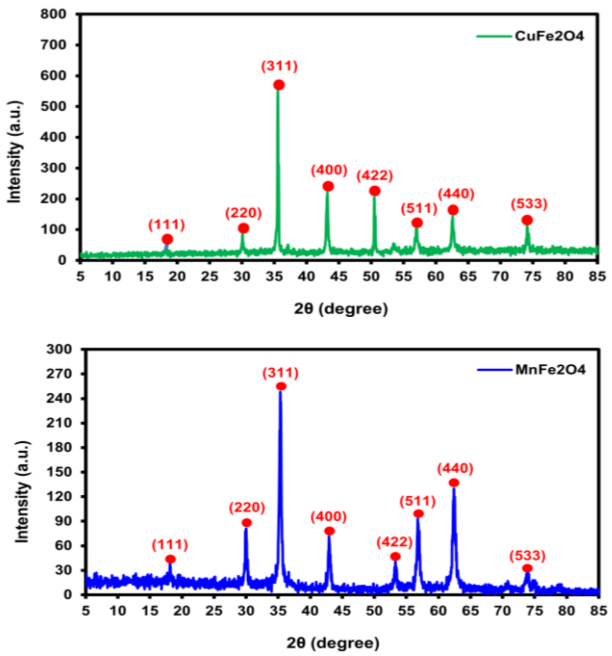

Figure 4. XRD analysis of $CuFe_2O_4$ and $MnFe_2O_4$ nanoparticles

3.5. VSM properties of $CuFe_2O_4$ and $MnFe_2O_4$ NPs

The magnetic properties of NPs were examined within a field range of -10,000 to +10,000 Oe. The $CuFe_2O_4$ and $MnFe_2O_4$ NPs exhibited the saturation magnetization values of 14.88 emu/g and 31.95 emu/g, respectively. Magnetic behavior typically depends on several factors, including particle shape, size, and crystallinity. Given the similar morphology and crystal structures obtained for $CuFe_2O_4$ and $MnFe_2O_4$, it is suggested that the type of metal, and possibly NP size, may be significant parameters influencing the magnetic properties [28-30].

3.6. MTT analysis

The MTT assay evaluated the cytotoxicity of $CuFe_2O_4$ and $MnFe_2O_4$ NPs at varying concentrations (0.01–0.2 mg/mL) on cell viability (%). $CuFe_2O_4$ exhibited significantly higher cytotoxicity than $MnFe_2O_4$ with increasing concentrations, leading to a greater reduction in cell viability (Fig. 6).

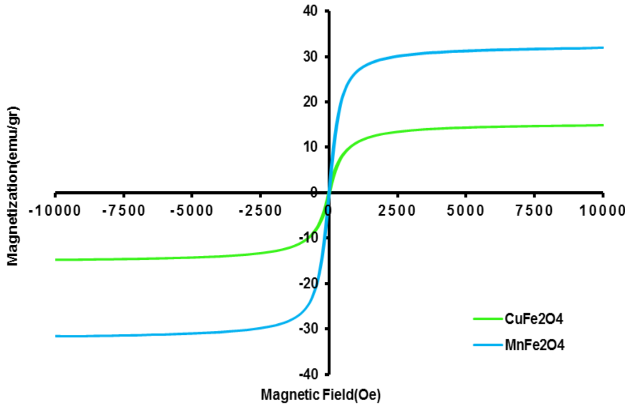

Figure 5. VSM analysis of $CuFe_2O_4$ and $MnFe_2O_4$ nanoparticles

A comparison of $CuFe_2O_4$-treated cells across different concentrations revealed a significant difference relative to the control group (**** $P < 0.0001$). As shown in Fig. 6A, $MnFe_2O_4$, with a half-maximal inhibitory concentration (IC_{50}) value of 0.275 mg/mL, did not exert any anticancer effect on MCF-7 cells within the tested range (0.01–0.2 mg/mL), whereas $CuFe_2O_4$ displayed dose-dependent cytotoxicity with an IC_{50} value of 0.219 mg/mL. Remarkably, cell viability dropped below 60% at 0.1 mg/mL of $CuFe_2O_4$ compared to the $MnFe_2O_4$. This finding highlights the potential role of ferrite nanoparticles in cancer therapy. Previous studies have reported the therapeutic effect of MFe_2O_4 NPs on various cancer cell lines. For instance, Kanagesan et.al synthesized $MnFe_2O_4$ magnetic NPs via a sol-gel self-combustion method using iron and manganese nitrates, after calcination (150 °C for 24 h). Characterization by XRD, FTIR, TEM, and VSM confirmed a single-phase spinel structure, nanoscale dimensions, and favorable magnetic properties. The NPs exhibited dose-dependent cytotoxicity against murine mammary carcinoma breast cancer cells (4T1), with IC_{50} values decreasing from 210 µg/mL (24 h) to 171 µg/mL (72 h). Higher concentrations induced apoptosis and necrosis, whereas concentrations below 125 µg/mL displayed greater biocompatibility, highlighting their potential biomedical applications, especially in cancer therapy [28].

As noted above, although $MnFe_2O_4$ displays higher saturation magnetization, $CuFe_2O_4$ is more cytotoxic. This difference could be attributed to the enhanced ROS generation, metal ion release under physiological conditions, plasma membrane disruption, and mitochondrial dysfunction. Both copper and manganese ions can participate in Fenton-like reactions, producing hydroxyl radicals more rapidly and effectively than Mn or Fe. Under identical H_2O_2 levels, Cu-containing nanoparticles typically induce stronger oxidative stress. Furthermore, Cu^{2+} and $Fe^{2+/3+}$ can be released into acidic lysosomal compartments (pH ≈ 4.5) or culture media, directly damaging proteins and DNA. Cu^{2+} is released more rapidly and extensively than Mn^{2+} in acidic intracellular environments. Free copper ions react with protein thiols, disturb iron metabolism, and cause DNA damage, whereas Mn^{2+}, at physiological concentrations, generally exerts weaker toxic effects. Uncoated or highly charged NPs can further increase the membrane permeability, resulting in cell lysis and reduced cell viability. Copper ions interact more readily with membrane phospholipids and amino/thiol groups, accelerating membrane compromise [13, 31].

In line with earlier reports (Table 1), Islam et al. synthesized chitosan-coated $MnFe_2O_4$ via co-precipitation and assessed its cytotoxicity against human cervical carcinoma cells (HeLa); however, they did not evaluate uncoated $MnFe_2O_4$ or $CuFe_2O_4$ in MCF-7 cells [32]. Srikanth et al. synthesized $CuFe_2O_4$ hydrothermally and evaluated their cytotoxicity on catfish ovary cells (CCO); however, MCF-7 cells were not investigated [33]. Manh et al. prepared $MnFe_2O_4$–Ag hybrid NPs via co-precipitation and assessed their cytotoxicity in HepG2 and HeLa cells; however, pure $CuFe_2O_4$ or $MnFe_2O_4$ were not examined, and the hydrothermal synthesis method was not employed [34]. Ahamed et al. reported the cytotoxicity of $CuFe_2O_4$ on MCF-7 cells, while $CuFe_2O_4$ was synthesized under different co-precipitation conditions. Moreover, $MnFe_2O_4$ NPs were not evaluated in this study [13]. As summarized in Table 2, none of these studies conducted a direct, head-to-head comparison of both ferrites synthesized hydrothermally under identical reaction conditions using the same cancer cell model.

Table 2. Comparison of different ferrite nanoparticles for cancer therapy

Nanoparticle	Cell line	IC50	Cytotoxic effects	Applications	Ref.
$CuFe_2O_4$	MCF-7	100 µg/mL	Up-regulation of caspase-3 and caspase-9 genes; oxidative stress	Cancer therapy	[13]
$Cu_{0.5}Zn_{0.5}Fe_2O_4$	MG63	-	Heating	Hyperthermia	[14]
CS-$Mg_{0.5}Co_{0.5}Fe_2O_4$-5FU	HEK293 MCF-7 HeLa	251 µg/mL 158 µg/mL 158 µg/mL	5-FU, RNA, and DNA damage	Drug delivery	[15]
Ca^{2+}-doped $MgFe_2O_4$	MDA-MB-231	-	Laser-irradiated	Cancer Photothermal therapy	[18]
$Mn_{0.5}Zn_{0.5}Fe_2O_4$	HCC	-	Heating	Hyperthermia	[22]
$NiZnFe_2O_4$	HT29 MCF-7 HepG2	15.6–1,000 µg/mL	Caspase-3 and -9 activities and DNA fragmentation	Cancer therapy	[23]
$NiFe_2O_4$	MCF-7 HepG2	5–25 µg/ml	ROS generation, lipid peroxidation, Higher activity of caspase-3 and caspase-9	MRI, Drug delivery, and Cancer hyperthermia	[24]
$ZnFe_2O_4$	A549 A431 HepG2	10–40 µg/ml	Oxidative stress (ROS and GSH); higher activity of caspase-3 and caspase-9	Cancer therapy	[25]
$MgFe_2O_4$	MCF-7	400 µg /mL	-	Cancer therapy	[27]
$MnFe_2O_4$	4T1	210 µg /mL	-	Drug carrier agents	[28]
MB-$CuFe_2O_4$	Hela	50 ppm	Fenton catalyst to convert hydrogen peroxide (H_2O_2) into ROS	MRI, Photodynamic therapy	[31]
$MnFe_2O_4$-Ag	HepG2 HeLa	83±5.6 µg/mL 122.6±19.8 µg/mL	Heating	Hyperthermia	[34]

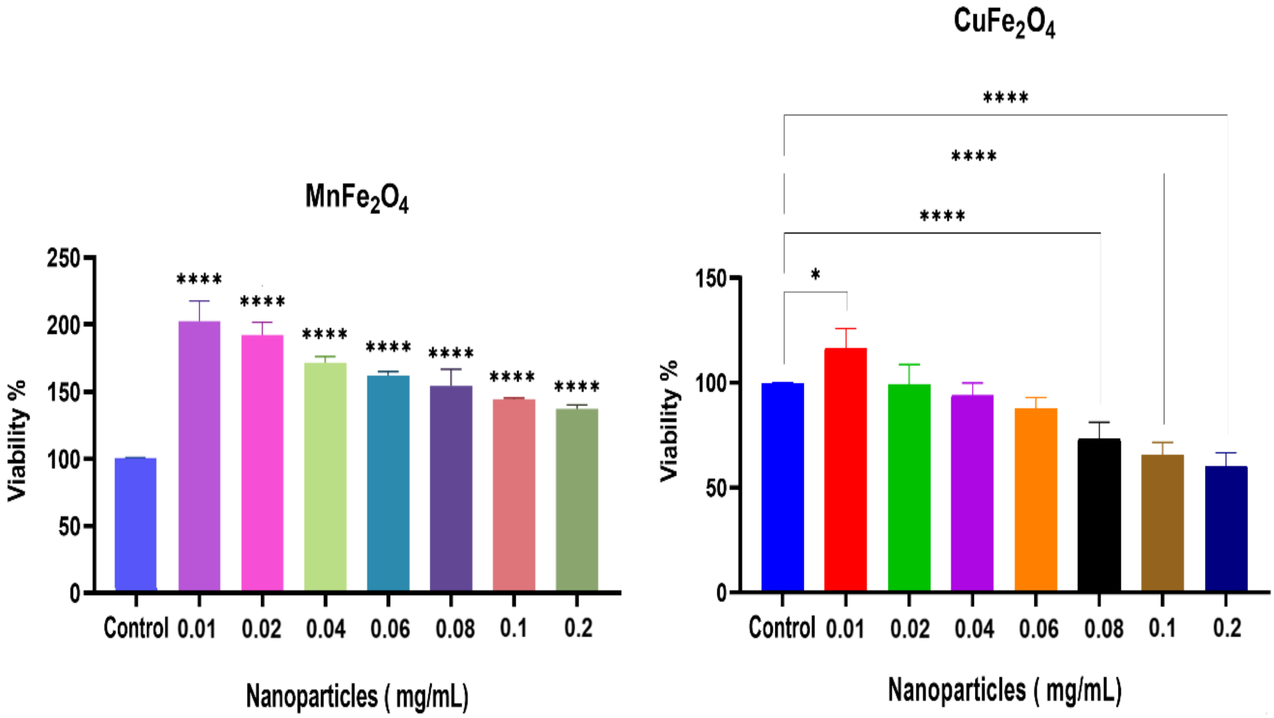

Figure 6. MTT assay results showing the viability (%) of the MCF-7 cell line following exposure to varying concentrations of $CuFe_2O_4$ and $MnFe_2O_4$ NPs. Data are expressed as the mean ± SD ($n = 3$ independent biological replicates). *$p < 0.05$; ****$p < 0.0001$ indicate the significant differences compared with untreated control cells, as determined by one-way ANOVA followed by Newman-Keuls multiple comparison post-hoc tests

4. Conclusion

This study successfully synthesized $CuFe_2O_4$ and $MnFe_2O_4$ nanoparticles (NPs) via a hydrothermal method, resulting in spherical morphologies with average diameters of approximately 145 nm and 170 nm, respectively. Characterization confirmed the structural, optical, and magnetic properties of the materials, with XRD revealing pure-phase spinel structures and EDX validating the stoichiometric compositions. UV–Vis spectra showed characteristic charge-transfer peaks, while VSM measurements indicated higher saturation magnetization for $MnFe_2O_4$ (31.95 emu/g) compared to $CuFe_2O_4$ (14.88 emu/g). MTT assays demonstrated significant dose-dependent cytotoxicity in MCF-7 cells, with $CuFe_2O_4$ exhibiting greater toxicity than $MnFe_2O_4$. These findings highlight $CuFe_2O_4$ NPs as promising candidates for further biomedical research, particularly in targeted cancer therapy.

Acknowledgements

The kind assistance of the Motamed Cancer Institute and Riz Afzar Sazan Ayandeh Biotechnology Co. (RASA Biotech Co.) is acknowledged.

Funding

This research did not receive any specific grant from funding agencies in the public, commercial, or not-for-profit sectors. The study was self-funded by the first author.

Authors Contribution

All authors undertook the conception and design of the study. Mehdi Abdollahzadeh Parsa performed material preparation, data collection, and analysis. Mehdi Abdollahzadeh Parsa prepared the first draft of the manuscript, and all authors provided comments on previous versions of the manuscript. The final version of the manuscript was read and approved by all authors.

Availability of data and materials:

The datasets generated and/or analyzed during the current study are available from the corresponding author on reasonable request.

Conflict of interests

The authors declare that they have no known financial or personal relationships that could have appeared to influence the work reported in this paper.

References

[1] Eivazzadeh-Keihan R, Bahreinizad H, Amiri Z, Aliabadi HA, Salimi-Bani M, Nakisa A, Davoodi F, Tahmasebi B, Ahmadpour F, Radinekiyan F, Maleki A. Functionalized magnetic nanoparticles for the separation and purification of proteins and peptides. *TrAC Trends in Analytical Chemistry*. 2021 Aug 1; 141:116291. doi.org/10.1016/j.trac.2021.116291

[2] Williams HD, Trevaskis NL, Charman SA, Shanker RM, Charman WN, Pouton CW, Porter CJ. Strategies to address low drug solubility in discovery and development. *Pharmacological reviews*. 2013 Jan 1;65(1):315-499. doi.org/10.1124/pr.112.005660

[3] Du JZ, Du XJ, Mao CQ, Wang J. Tailor-made dual pH-sensitive polymer–doxorubicin nanoparticles for efficient anticancer drug

delivery. *Journal of the American Chemical Society*. 2011 Nov 9;133(44):17560-3. doi.org/10.1021/ja207150n

[4] Firdhouse MJ, Lalitha P. Flower-shaped gold nanoparticles synthesized using Kedrostis foetidissima and their antiproliferative activity against bone cancer cell lines. *International Journal of Industrial Chemistry*. 2016 Dec;7(4):347-58. doi.org/10.1007/s40090-016-0098-4

[5] Wilson B, Geetha KM. Nanomedicine to deliver biological macromolecules for treating COVID-19. *Vaccine*. 2022 Jun 23;40(29):3931-41. doi.org/10.1016/j.vaccine.2022.05.068

[6] Kefayat A, Sartipzadeh O, Molaabasi F, Amiri M, Gholami R, Mirzadeh M, Shokati F, Khandaei M, Ghahremani F, Poursamar SA, Sarrami-Forooshani R. Microfluidic system consisting of a magnetic 3d-printed microchannel filter for isolation and enrichment of circulating tumor cells targeted by anti-HER2/MOF@ ferrite core–shell nanostructures: a theranostic CTC dialysis system. *Analytical Chemistry*. 2024 Mar 5;96(11):4377-84. doi.org/10.1021/acs.analchem.3c03567

[7] Gharehdaghi Z, Naghib SM, Rahimi R, Bakhshi A, Kefayat A, Shamaeizadeh A, Molaabasi F. Highly improved pH-Responsive anticancer drug delivery and T2-Weighted MRI imaging by magnetic MOF CuBTC-based nano/microcomposite. *Frontiers in Molecular Biosciences*. 2023 Apr 4; 10:1071376. doi.org/10.3389/fmolb.2023.1071376

[8] Amiri M, Salavati-Niasari M, Akbari A. Magnetic nanocarriers: evolution of spinel ferrites for medical applications. *Advances in colloid and interface science*. 2019 Mar 1; 265:29-44. doi.org/10.1016/j.cis.2019.01.003

[9] Ko MJ, Min S, Hong H, Yoo W, Joo J, Zhang YS, Kang H, Kim DH. Magnetic nanoparticles for ferroptosis cancer therapy with diagnostic imaging. *Bioactive Materials*. 2024 Feb 1; 32:66-97. doi.org/10.1016/j.bioactmat.2023.09.015

[10] Ojha VH, Oza AH, Agrawal R, Ningthoujam RS. Classification of Ferrites, Synthesis and Properties of Spinel Ferrite Nanoparticles and Their Applications. In Handbook of Materials Science, Volume 2: Magnetic Materials 2024 Aug 16 (pp. 103-146). Singapore: *Springer Nature Singapore*. doi.org/10.1007/978-981-97-4646-0_4

[11] Zhao J. Effect of Magnesium Ferrite on Highly Selective Phenol Hydroxylation Catalyst. *International Journal of Industrial Chemistry*. 2024 Mar 15;15(1). doi.org/10.57647/j.ijic.2024.1501.07

[12] Kharisov BI, Dias HR, Kharissova OV. Mini-review: Ferrite nanoparticles in the catalysis. *Arabian Journal of Chemistry*. 2019 Nov 1;12(7):1234-46. doi.org/10.1016/j.arabjc.2014.10.049

[13] Ahamed M, Akhtar MJ, Alhadlaq HA, Alshamsan A. Copper ferrite nanoparticle-induced cytotoxicity and oxidative stress in human breast cancer MCF-7 cells. Colloids and Surfaces B: *Biointerfaces.* 2016 Jun 1; 142:46-54. doi.org/10.1016/j.colsurfb.2016.02.043

[14] Al-Gburi HH, Hassanzadeh-Tabrizi SA, Jabbarzare S. Production of Cu0. 5Zn0. 5Fe2O4 Nanostructures as a Hyperthermia Agent for Cancer Healing. *International Journal of Biomaterials*. 2025;2025(1):7290633. doi.org/10.1155/ijbm/7290633

[15] Mngadi S, Mokhosi S, Singh M, Mdlalose W. Chitosan-functionalized Mg0. 5Co0. 5Fe2O4 magnetic nanoparticles enhance delivery of 5-fluorouracil in vitro. *Coatings*. 2020 May 2;10(5):446. doi.org/10.3390/coatings10050446

[16] Faisal F, Tatarinova G, Mukhamadjon Ugli TD, Abdugabbarovna DL, Ikhtiyorovna KD, Normuminovna KD, Boynazarovich MR, Sapaev IB, Rasulovna RM, Komil Ugli KJ, Aliyorovna GJ. Magnetic Nanoparticles for Targeted Drug Delivery in a Mouse Model of Breast Cancer. *Journal of Nanostructures*. 2024 Jan 1;14(1):101-8. doi.org/10.22052/JNS.2024.01.010

[17] Wu M, Huang S. Magnetic nanoparticles in cancer diagnosis, drug delivery and treatment. *Molecular and clinical oncology*. 2017 Nov 1;7(5):738-46. doi.org/10.3892/mco.2017.1399

[18] Manivasagan P, Ashokkumar S, Manohar A, Joe A, Han HW, Seo SH, Thambi T, Duong HS, Kaushik NK, Kim KH, Choi EH. Biocompatible calcium ion-doped magnesium ferrite nanoparticles as a new family of photothermal therapeutic materials for cancer treatment. *Pharmaceutics*. 2023 May 21;15(5):1555. doi.org/10.3390/pharmaceutics15051555

[19] Jauhar S, Kaur J, Goyal A, Singhal S. Tuning the properties of cobalt ferrite: a road towards diverse applications. *RSC advances*. 2016;6(100):97694-719. doi.org/10.1039/C6RA21224G

[20] Kückelhaus S, Reis SC, Carneiro MF, Tedesco AC, Oliveira DM, Lima EC, Morais PC, Azevedo RB, Lacava ZG. In vivo investigation of cobalt ferrite-based magnetic fluid and magnetoliposomes using morphological tests. *Journal of magnetism and magnetic materials*. 2004 May 1; 272:2402-3. doi.org/10.1016/j.jmmm.2003.12.1218

[21] Baldi G, Bonacchi D, Innocenti C, Lorenzi G, Sangregorio C. Cobalt ferrite nanoparticles: The control of the particle size and surface state and their effects on magnetic properties. *Journal of Magnetism and Magnetic Materials*. 2007 Apr 1;311(1):10-6. doi.org/10.1016/j.jmmm.2006.11.157

[22] Lin M, Zhang D, Huang J, Zhang J, Xiao W, Yu H, Zhang L, Ye J. The anti-hepatoma effect of nanosized Mn–Zn ferrite magnetic fluid hyperthermia associated with radiation in vitro and in vivo. *Nanotechnology*. 2013 May 24;24(25):255101. doi.org/10.1088/0957-4484/24/25/255101

[23] Al-Qubaisi MS, Rasedee A, Flaifel MH, Ahmad SH, Hussein-Al-Ali S, Hussein MZ, Eid EE, Zainal Z, Saeed M, Ilowefah M, Fakurazi S. Cytotoxicity of nickel zinc ferrite nanoparticles on cancer cells of epithelial origin. *International journal of nanomedicine*. 2013 Jul 15:2497-508. doi.org/10.2147/IJN.S42367

[24] Ahamed M, Akhtar MJ, Alhadlaq HA, Khan MM, Alrokayan SA. Comparative cytotoxic response of nickel ferrite nanoparticles in human liver HepG2 and breast MFC-7 cancer cells. *Chemosphere*. 2015 Sep 1; 135:278-88. doi.org/10.1016/j.chemosphere.2015.03.079

[25] Alhadlaq HA, Akhtar MJ, Ahamed M. Zinc ferrite nanoparticle-induced cytotoxicity and oxidative stress in different human cells. *Cell & bioscience*. 2015 Sep 17;5(1):55. doi.org/10.1186/s13578-015-0046-6

[26] Vurro F, Gerosa M, Busato A, Muccilli M, Milan E, Gaudet J, Goodwill P, Mansfield J, Forlin E, Negri A, Gherlinzoni F. Doped ferrite nanoparticles exhibiting self-regulating temperature as magnetic fluid hyperthermia antitumoral agents, with diagnostic capability in magnetic resonance imaging and magnetic particle *imaging. Cancers*. 2022 Oct 20;14(20):5150. doi.org/10.3390/cancers14205150

[27] Kanagesan S, Hashim M, Tamilselvan S, Alitheen NB, Ismail I, Bahmanrokh G. Cytotoxic effect of nanocrystalline MgFe2O4 particles for cancer cure. *Journal of Nanomaterials*. 2013;2013(1):865024. doi.org/10.1155/2013/865024

[28] Kanagesan S, Aziz SB, Hashim M, Ismail I, Tamilselvan S, Alitheen NB, Swamy MK, Purna Chandra Rao B. Synthesis, characterization and in vitro evaluation of manganese ferrite (MnFe2O4) nanoparticles for their biocompatibility with murine

breast cancer cells (4T1). *Molecules*. 2016 Mar 11;21(3):312. doi.org/10.3390/molecules21030312

[29] Rafique MY, Pan LQ, Iqbal MZ, Qiu HM, Farooq MH, Guo ZG, Tanveer M. Growth of monodisperse nanospheres of MnFe2O4 with enhanced magnetic and optical properties. *Chinese Physics* B. 2013 Oct 1;22(10):107101. doi.org/10.1088/1674-1056/22/10/107101

[30] Deraz NM, Alarifi A. Controlled synthesis, physicochemical and magnetic properties of nano-crystalline Mn ferrite system. *International Journal of Electrochemical Science*. 2012 Jan 1;7(6):5534-43. doi.org/10.1016/S1452-3981(23)19640-4

[31] Kuo SH, Wu PT, Huang JY, Chiu CP, Yu J, Liao MY. Fabrication of anisotropic Cu ferrite-polymer core-shell nanoparticles for photodynamic ablation of cervical cancer cells. *Nanomaterials*. 2020 Dec 4;10(12):2429. doi.org/10.3390/nano10122429

[32] Islam K, Haque M, Kumar A, Hoq A, Hyder F, Hoque SM. Manganese ferrite nanoparticles (MnFe2O4): size dependence for hyperthermia and negative/positive contrast enhancement in MRI. *Nanomaterials*. 2020 Nov 20;10(11):2297. doi.org/10.3390/nano10112297

[33] Srikanth K, Nutalapati V. Copper ferrite nanoparticles induced cytotoxicity and oxidative stress in Channel catfish ovary cells. *Chemosphere*. 2022 Jan 1; 287:132166. doi.org/10.1016/j.chemosphere.2021.132166

[34] Nha TT, Nam PH, Phuc NX, Nguyen VQ, Nam NH, Manh DH, Tam LT, Linh NT, Khanh BT, Lu LT, Nguyen LH. Sensitive MnFe 2 O 4–Ag hybrid nanoparticles with photothermal and magnetothermal properties for hyperthermia applications. *RSC advances*. 2021;11(48):30054-68. doi.org/10.1039/D1RA03216J